Farhan, Alan; Saccone, Michael; Petersen, Charlotte; Dhuey, Scott; Hofhuis, Kevin; Mansell, Rhodri; Chopdekar, Rajesh V.; Scholl, Andreas; Lippert, Thomas; van Dijken, Sebastiaan

Geometrical Frustration and Planar Triangular Antiferromagnetism in Quasi-Three-Dimensional Artificial Spin Architecture

Published in:
Physical Review Letters

DOI:
10.1103/PhysRevLett.125.267203

Published: 30/12/2020

Document Version
Publisher's PDF, also known as Version of record

Please cite the original version:
Farhan, A., Saccone, M., Petersen, C., Dhuey, S., Hofhuis, K., Mansell, R., Chopdekar, R. V., Scholl, A., Lippert, T., & van Dijken, S. (2020). Geometrical Frustration and Planar Triangular Antiferromagnetism in Quasi-Three-Dimensional Artificial Spin Architecture. *Physical Review Letters*, *125*(26), Article 267203. https://doi.org/10.1103/PhysRevLett.125.267203

Geometrical Frustration and Planar Triangular Antiferromagnetism in Quasi-Three-Dimensional Artificial Spin Architecture

Alan Farhan,[1,2,3,*] Michael Saccone,[1,4] Charlotte F. Petersen,[5] Scott Dhuey,[6] Kevin Hofhuis,[2,7] Rhodri Mansell,[1] Rajesh V. Chopdekar,[3] Andreas Scholl,[3] Thomas Lippert,[2,8] and Sebastiaan van Dijken[1]

[1]*NanoSpin, Department of Applied Physics, Aalto University School of Science, P.O. Box 15100, FI-00076 Aalto, Finland*
[2]*Laboratory for Multiscale Materials Experiments (LMX), Paul Scherrer Institut, 5232 Villigen, Switzerland*
[3]*Advanced Light Source, Lawrence Berkeley National Laboratory, One Cyclotron Road, Berkeley, California 94720, USA*
[4]*Physics Department, University of California, 1156 High Street, Santa Cruz, California 95064, USA*
[5]*Institut für Theoretische Physik, Universität Innsbruck, Technikerstraße 21A, A-6020 Innsbruck, Austria*
[6]*Molecular Foundry, Lawrence Berkeley National Laboratory, One Cyclotron Road, Berkeley, California 94720, USA*
[7]*Laboratory for Mesoscopic Systems, Department of Materials, ETH Zurich, 8093 Zurich, Switzerland*
[8]*Department of Chemistry and Applied Biosciences, Laboratory of Inorganic Chemistry, ETH Zurich, 8093 Zurich, Switzerland*

(Received 30 June 2020; revised 1 October 2020; accepted 4 December 2020; published 30 December 2020)

We present a realization of highly frustrated planar triangular antiferromagnetism achieved in a quasi-three-dimensional artificial spin system consisting of monodomain Ising-type nanomagnets lithographically arranged onto a deep-etched silicon substrate. We demonstrate how the three-dimensional spin architecture results in the first direct observation of long-range ordered planar triangular antiferromagnetism, in addition to a highly disordered phase with short-range correlations, once competing interactions are perfectly tuned. Our work demonstrates how escaping two-dimensional restrictions can lead to new types of magnetically frustrated metamaterials.

DOI: 10.1103/PhysRevLett.125.267203

Artificial frustrated spin systems comprising monodomain Ising-type nanomagnets lithographically arranged onto a variety of two-dimensional lattices enable direct visualization of geometrical spin frustration and its fascinating consequences. Prominent examples, among others [1,2], include emergent magnetic monopoles in macroscopically degenerate artificial spin ice [3,4], vertex frustration [5–7], polaronic states [6,8], field-induced phase coexistence [9], topological frustration [10,11], and the first steps towards artificial spin glasses [12,13]. Proposed applications range from user-defined writing and manipulation of magnetic configurations [14,15] to reconfigurable magnonic band structures [16]. In all of these examples, freedom within the two-dimensional space is used to design systems that feature desired properties or emergent phenomena of interest, whether it is in restoring spin ice degeneracy in artificial square ice [17,18], lifting spin ice degeneracy in artificial kagome spin ice [19], or all other aforementioned examples. However, the restriction to two-dimensional lattices limits the number of naturally occurring phenomena that can be modeled by such artificial systems. For instance, a prominent example of spin frustration occurring in nature, the triangular antiferromagnet [20–22], has not yet found an artificial classical analog that exhibits thermally driven moment fluctuations, thus impeding the direct visualization of the statistical physics of triangular antiferromagnetism. The only two-dimensional triangular antiferromagnets are quasifrozen systems exhibiting out-of-plane spins [23,24]. In addition, a geometrically frustrated system analog to a triangular antiferromagnet has been explored using close-packed colloidal spheres between parallel walls [25]. There, in-plane lattice distortions tend to relieve the ground state degeneracy, resulting in long-range ordered patterns. This raises the question of whether an artificial triangular antiferromagnet can be created that exhibits an extensive ground state degeneracy and allows for thermal fluctuations at accessible temperatures, as it will allow for a direct visualization of the statistical physics of highly frustrated triangular antiferromagnetism.

Here, we report the first realization of an artificial analogue to a planar triangular antiferromagnet that exhibits thermally induced moment fluctuations. We achieve this by placing parallel chains of Ising-type nanomagnets on top of a deep-etched silicon (100) substrate [4] (see also Supplemental Material [26]), which breaks the two-dimensional barrier by introducing variable height offsets h between neighboring nanomagnets [Figs. 1(a), 1(b)]. One set of nanomagnets [blue framed nanomagnet in Fig. 1(a)] is grown on top of etched plateaus [deep yellow frame in Fig. 1(a)], while the other set is grown on the base of the substrate [red framed nanomagnet in Fig. 1(a)]. In addition to the height offset h, the collinear center-to-center nanomagnet distance b is lithographically tuned [see b in Fig. 1(a)]. In other words, we are generating a rectangular lattice consisting of two sublattices which are increasingly

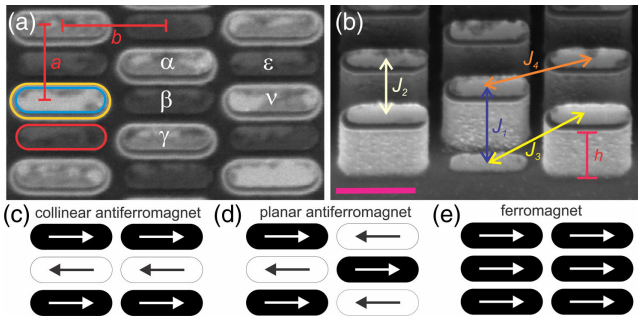

FIG. 1. (a) Scanning electron microscopy image of an artificial triangular antiferromagnetic lattice consisting of nanomagnets (length = 400 nm, width = 100 nm) placed on a deep-etched silicon substrate (top view). One set of nanomagnets (blue frame) is placed on top of etched plateaus (deep yellow frame), while another set of nanomagnets (red frame) is patterned on the base of the substrate. The lattice parameter $a = 330$ nm is kept constant, while b is varied between 475 and 680 nm. (b) Side-view SEM image highlighting how competing interactions J_1 to J_4 vary by changing h and b. The magenta-colored bar indicates a length of 400 nm. (c)–(e) Illustration of collinear antiferromagnetic (c), planar antiferromagnetic (d), and ferromagnetic ordering (e).

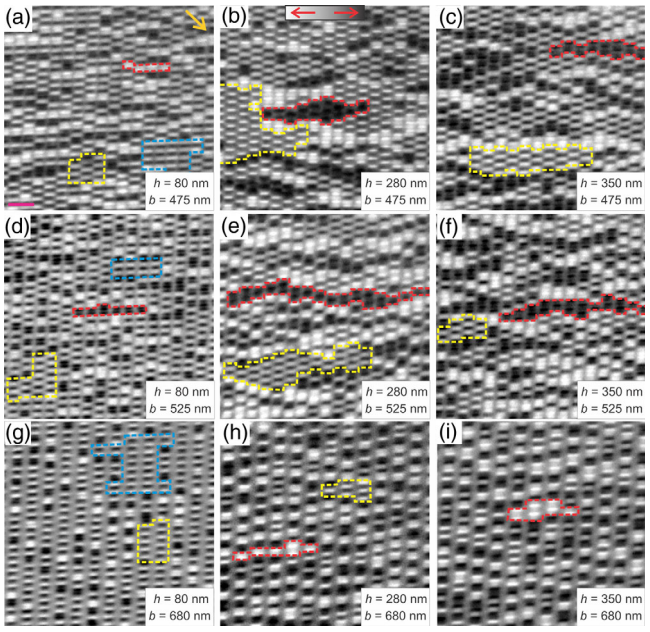

FIG. 2. (a)–(i) XMCD images of frozen-in configurations ($T = 150$ K) for structures with various height offsets ($h = 80$, 280, and 350 nm) and lattice parameters ($b = 475$, 525, and 680 nm). Moments pointing towards the incoming x-rays (deep yellow arrow) appear dark, while moments opposing the incoming x rays appear bright, as illustrated in the dark-and-bright color bar on top of (b). The magenta-colored bar in (a) indicates a length of 1 μm. Dashed blue, yellow, and red frames highlight collinear antiferromagnetic, planar antiferromagnetic, and ferromagnetic domains, respectively.

separated into different planes and whose mutual interaction is adjusted by varying both h and b. In purely two-dimensional systems ($h = 0$ nm), such arrays are known to exhibit long-range ordered collinear antiferromagnetic domains consisting of antiparallel chains of magnetic moments [12,27] [see Fig. 1(c)]. Magnetic ordering in our spin lattice with $h \neq 0$ nm is best understood by considering the competing interactions involved [see Fig. 1(b)]: J_1 and J_2 are antiferromagnetic in nature, involving nearest- [α and β in Fig. 1(a)] and next-nearest-neighbor parallel nanomagnets [α and γ in Fig. 1(a)], with their balance being directly controlled by the height offset h. J_3 and J_4 [Fig. 1(b)] are ferromagnetic in nature involving collinear [α and ϵ in Fig. 1(a)] and coplanar nearest neighbors [α and ν in Fig. 1(a)], respectively. The balance between these interactions is controlled both by the height offset h and lattice parameter b [Fig. 1(a)]. An increasing height offset adds a rising triangular coordination to J_1 and J_2 [Fig. 1(b)] and their strengths equalize at a critical offset h_c [Supplemental Material [26], Fig. 1(c)]. While this condition resembles the spin frustration and ground state degeneracy of triangular antiferromagnets [Supplemental Material [26], Figs. 1(a), 1(d)], two more competing interactions between spins within the two planar sublattices need to be taken into account. Ferromagnetic J_3 is controlled both through h and b, while coplanar J_4 is tuned by a variation of b [see Figs. 1(a), 1(b)]. Considering these competing interactions and the possibility of varying both h and b, it is expected that the quasi-three-dimensional artificial structure exhibits a considerable variation of possible spin configurations (see Supplemental Material [26], Fig. 2), as both parameters are varied. Prior to sample fabrication, we used micromagnetic simulations [28] (see also Ref. [26]) to determine the critical height offset to be $h_c = 280$ nm [see $J_1 = J_2$ in Supplemental Material [26], Fig. 1(c)] and show how J_3 and J_4 vary as a function of b for structures possessing various height offsets (Supplemental Material [26], Fig. 3). We directly visualize the magnetic configurations and thermal fluctuations in our system using cryogenic x-ray photoemission electron microscopy (X-PEEM) [29], employing x-ray magnetic circular dichroism (XMCD) at the Fe $L3$ edge [30].

As a first step, we apply a thermal annealing protocol that has previously shown to be effective in accessing low-energy configurations [4,8,31,32]. For this purpose, a set of samples was prepared with a blocking temperature $T_B = 200$–240 K, where we define T_B as the temperature where thermally driven moment reorientations within the patterned nanomagnets occur at a timescale of acquiring a single XMCD image (7–10 sec per image) [8,32]. Lattice parameter $a = 330$ nm is fixed [Fig. 1(a)], while b and h are varied. Following sample fabrication, the sample is kept in high vacuum at room temperature (300 K) for several days. After this, it is transferred into the PEEM and cooled down to 150 K, so that quasifrozen low-energy magnetic configurations are imaged [see Figs. 2(a)–2(i)].

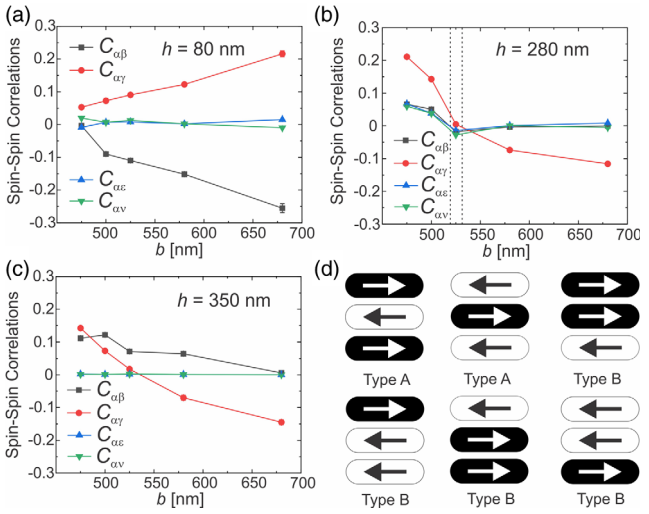

FIG. 3. (a)–(c) Nearest-neighbor spin correlation measures for artificial triangular antiferromagnets plotted as a function of lattice parameter b with height offsets of 80, 280, and 350 nm, respectively. (d) Trident types that obey a quasi-ice rule of two moments pointing left and one right or vice versa.

In the magnetic configurations achieved after thermal annealing [Figs. 2(a)–2(i)], we observe clear transitions as both h and b are varied. At a small lattice parameter ($b = 475$ nm), we find a transition from a dominance of collinear antiferromagnetic patterns [blue frame in Fig. 2(a)] at a low height offset ($h = 80$ nm), to growing ferromagnetic and planar antiferromagnetic ordering as the height offset increases [red and yellow frames in Figs. 2(b), 2(c)]. As we increase b to 525 nm, we observe a similar transition [see Figs. 2(d)–2(f)], but with one distinct feature at $h = 280$ nm (critical offset) that the mixing of ferromagnetic and planar antiferromagnetic order becomes more evident, as domains of both ordering types emerge with comparable sizes [Fig. 2(e)]. At larger values of the b parameter, the columns of nanomagnets start to decouple and ordering within individual columns becomes more random as the height offset increases [Figs. 2(g)–2(i)]. While collinear antiferromagnetic domain patterns have been observed in various two-dimensional artificial spin systems [6,27,33], it is the first time that a planar triangular antiferromagnetic phase is realized in an artificial spin system.

The visual observations are quantified by spin correlation measures of nearest- and next-nearest neighbor magnetic moments [34–36]. Figure 3(a) depicts correlation functions for spin structures with increasing b and a constant height offset $h = 80$ nm. The most striking feature is the opposing trends of $C_{\alpha\beta}$ and $C_{\alpha\gamma}$, while $C_{\alpha\epsilon}$ and $C_{\alpha\nu}$ remain close to zero for all values of b. As b increases, the influence of the ferromagnetic couplings J_3 and J_4 diminish (see Supplemental Material [26], Fig. 3), which leads to an increase in antiferromagnetic ordering along the columns of nanomagnets. In other words, tiles of so-called type A tridents [32] [see Fig. 3(d)] become more dominant. Around the critical height offset ($h = 280$ nm), the trends can be best understood through the decreasing strength of J_4 with increasing b [see Supplemental Material [26], Fig. 3(b)], with the J_1 and J_2 couplings now equal in strength. For lower values of b, the ferromagnetic J_4 coupling is strong and favors an extensive multidomain planar antiferromagnetic phase, interspersed with smaller ferromagnetic patterns associated with tiles of type B, together with domain boundaries. This leads to more ferromagnetically leaning correlations for $C_{\alpha\gamma}$, $C_{\alpha\nu}$, and $C_{\alpha\epsilon}$. Around $b = 525$ nm, all spin-spin correlations equalize near to zero, strongly suggesting that the highest degree of ordering competition, spin frustration, and degeneracy is achieved at a combination of $h = 280$ and $b = 525$ nm. At larger values of b, J_4 becomes weaker and the degeneracy within the triangular chains becomes more relevant. This leads to type A and type B tridents [see Fig. 3(d)] dominating the configurational landscape, with an increasing trend towards short-range order. The degeneracy between type A and type B tridents (twice as much type B than type A) drives $C_{\alpha\gamma}$ negative due to there being four available type B trident states compared to only two possible type A tridents. In structures with a height offset $h = 350$ nm $C_{\alpha\beta}$ remains ferromagnetic (positive) for all values for b [Fig. 3(c)]. This tendency towards ferromagnetic ordering can be understood by the fact that ordering patterns now have to minimize both J_2 and J_4 simultaneously. Thus, type B tridents shown in Fig. 3(d) become more favorable and expectedly dominate. It is only tiles from these four trident types that can minimize both J_2 and J_4. These observations, in particular the highest degree of frustration at $h = 280$ and $b = 525$ nm, are confirmed by micromagnetic simulations of lattices with differing values of h and b (Supplemental Material [26], Fig. 3).

Focusing on the critical height offset $h = 280$ nm, we imaged the temperature dependence of moment fluctuations on two sets of structures with $b = 475$ and $b = 525$ nm, following a waiting period of five months at room temperature. This long waiting period was added to allow for long relaxation times expected due to the influence of fabrication-induced intrinsic disorder [31]. Representative XMCD image sequences of the two structures are shown in Supplemental Material [26], movies 1 and 2. The sample with $b = 475$ nm exhibits robust long-range planar antiferromagnetic order, interspersed by small ferromagnetic patterns. Visually, a dramatic change is observed for $b = 525$ nm, as neither ferromagnetic nor antiferromagnetic ordering patterns are able to dominate throughout all accessible temperatures. This transition from long- to short-range order is quantitatively characterized, when looking at the magnetic structure factors [3,4,17], which we extracted as a function of temperature (see Fig. 4). For the system with $b = 475$ nm, we see sharp peaks in the magnetic structure factors, which remain

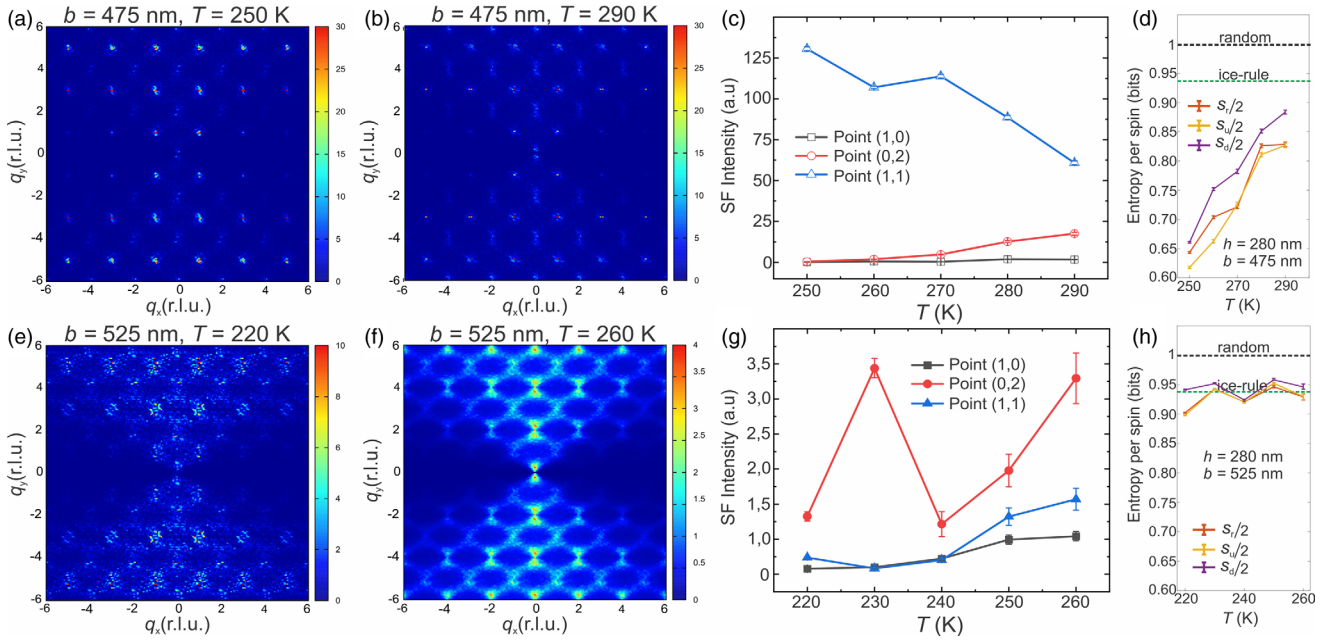

FIG. 4. (a),(b) Magnetic structure factors generated from moment configurations of a planar triangular antiferromagnet at a height offset of $h = 280$ nm and lattice parameter $b = 475$ nm, recorded at (a) $T = 250$ and (b) $T = 290$ K. (c) Structure factor intensities plotted as a function of temperature, at a chosen point in q space, for the $b = 475$ nm system. Chosen points (1,0), (0,2), and (1,1) reflect collinear antiferromagnetism, ferromagnetism, and planar antiferromagnetism, respectively. (d) Entropy density upper bounds plotted as a function of temperature. (e),(f) Magnetic structure factors for a highly frustrated system at the critical height offset of 280 nm and lattice parameter $b = 525$ nm, recorded at (e) $T = 220$ and (f) $T = 260$ K. (g) Same structure factor intensities as in (c). (h) Entropy densities for the highly frustrated case. The dashed lines in (d) and (h) are entropy upper bounds for perfectly random moment configurations (black dashed line) and random tiles of type A and type B (quasi-ice rule) tridents (green dashed line).

robust throughout all accessible temperatures [see Figs. 4(a), 4(b)]. Comparing these structure factors with those derived for a fully ordered planar antiferromagnet [see Supplemental Material [26], Fig. 4(a)], we see that the peaks overlap [see, e.g., the (1,1) point in Fig. 4(a), 4(b)], confirming long-range ordered planar antiferromagnetism. In addition to these peaks, we see contributions to the structure factors at points, for example at (0,2) in Fig. 4(a), that correspond to ferromagnetic ordering [compare with Supplemental Material [26], Fig. 4(c)]. Collinear antiferromagnetic ordering [compare to Supplemental Material [26], Fig. 4(b)] seems fully absent. Plotting structure factor intensities at points of interest as a function of temperature reveals an interesting trend, with the planar antiferromagnetic order gradually weakening [see open blue triangles in Fig. 4(c)] and ferromagnetic order moderately rising with temperature [see open red circles in Fig. 4(c)]. These trends are also reflected when plotting the population of the fourteen possible building-block ordering patterns (see Supplemental Material [26], Fig. 2) as a function of temperature [see Supplemental Material [26], Fig. 5(a)]. These long-range ordering patterns stand in contrast to those observed in the $b = 525$ nm structure. There, the magnetic structure factors appear far more diffuse [see Fig. 4(e)], strongly reflecting the high level of frustration-induced disorder in the system, as none of the ordering patterns is able to dominate. As the temperature rises, the population of several competing moment configurations rises [see Supplemental Material [26], Fig. 5(b)], leading to an even more diffuse structure factor [see Fig. 4(f)] and a collective rise in structure factor intensities at all the aforementioned points [see Fig. 4(g)]. To further illustrate these observations, we applied a method of direct entropy determination [26,37]. For $b = 475$ nm, entropies start at lower values and rise with increasing temperature [see Fig. 4(d)]. This stands in contrast to the $b = 525$ nm system, which remains stuck in a high-entropy phase, throughout all temperature regimes [see Fig. 4(h)]. Furthermore, when comparing these experimentally extracted entropy densities with those derived for totally randomized moment configurations [black dashed line in Figs. 4(d), 4(h)] and patterns with short-range order, the $b = 525$ nm system appears to fall within this "ice-rule" regime [see green dashed line Fig. 4(h)]. This confirms the persistent short-range ordering, when competing interactions are perfectly tuned.

At $b = 525$ nm each nanomagnet is coupled with equal strength to six other nanomagnets in the same plane, two antiferromagnetically and four ferromagnetically, along with two antiferromagnet couplings to nanomagnets in the other plane. Calculating the energies associated with various building-block moment configurations

(see Supplemental Material [26], Figs. 2 and 6), the planar antiferromagnet emerges as the expected ground state, for all values of b (and $h = 280$ nm), most crucially $b = 525$ nm. However, previous work on artificial kagome spin ice showed, that looking at ground state patterns in building block structures does not fully reflect ordering in extended arrays [36,38]. The observed robust coexistence of short-range ferro- and planar antiferromagnetic order places the ground state as an open question, that needs to be addressed in future work. The tunable competition between such ordering patterns and the high levels of competition-infused entropies will allow for a direct comparison to analog situations emerging in naturally occurring glassy systems [39] or newly emerging high-entropy oxide multiferroics [40], where ferro- and antiferromagnetic order compete for dominance.

In summary, we introduced a quasi-three-dimensional artificial frustrated spin system, which not only allows the first artificial realization of long-range ordered planar triangular antiferromagnetism, but can also get stuck in a highly disordered phase marked by short-range correlations, when competing interactions are perfectly tuned. Our results demonstrate how a quasi-three-dimensional spin architecture can generate novel geometrically frustrated and extensively degenerate spin systems that go beyond the archetypes of ice-rule obedience [34,36] and vertex dominated phenomena [5–7,11].

The authors thank O. Narayan for his support. This project was supported by the Swiss National Science Foundation (Project No. 174306), the Academy of Finland (Project No. 316857) and by the Aalto Centre for Quantum Engineering. K. H. acknowledges support from the Swiss National Science Foundation (Project No. 200020_172774). Part of this work was performed at the PEEM3 beam line at the Advanced Light Source and the cleanroom facilities at the Molecular Foundry, Lawrence Berkeley National Laboratory (LBNL). The Advanced Light Source and the Molecular Foundry are supported by the Director, Office of Science, Office of Basic Energy Sciences, of the U.S. Department of Energy under Contract No. DE-AC02-05CH11231.

*alan.farhan@gmx.net

[1] S. H. Skjærvø, C. H. Marrows, R. L. Stamps, and L. J. Heyderman, Nat. Rev. Phys. **2**, 13 (2020).
[2] N. Rougemaille and B. Canals, Eur. Phys. J. B **92**, 62 (2019).
[3] Y. Perrin, B. Canals, and N. Rougemaille, Nature (London) **540**, 410 (2016).
[4] A. Farhan, M. Saccone, C. F. Petersen, S. Dhuey, R. V. Chopdekar, Y.-L. Huang, N. Kent, Z. Chen, M. J. Alava, T. Lippert, A. Scholl, and S. van Dijken, Sci. Adv. **5**, eaav6380 (2019).
[5] I. Gilbert, G.-W. Chern, S. Zhang, L. O'Brien, B. Fore, C. Nisoli, and P. Schiffer, Nat. Phys. **10**, 670 (2014).
[6] M. Saccone, K. Hofhuis, Y.-L. Huang, S. Dhuey, Z. Chen, A. Scholl, R. V. Chopdekar, S. van Dijken, and A. Farhan, Phys. Rev. Mater. **3**, 104402 (2019).
[7] Y. Lao, F. Caravelli, M. Sheikh, J. Sklenar, D. Gardeazabal, J. D. Watts, A. M. Albrecht, A. Scholl, K. Dahmen, C. Nisoli, and P. Schiffer, Nat. Phys. **14**, 723 (2018).
[8] A. Farhan, A. Scholl, C. F. Petersen, L. Anghinolfi, C. Wuth, S. Dhuey, R. V. Chopdekar, P. Mellado, M. J. Alava, and S. van Dijken, Nat. Commun. **7**, 12635 (2016).
[9] J. Sklenar, Y. Lao, A. Albrecht, J. D. Watts, C. Nisoli, G.-W. Chern, and P. Schiffer, Nat. Phys. **15**, 191 (2019).
[10] J. Drisko, T. Marsh, and J. Cumings, Nat. Commun. **8**, 14009 (2017).
[11] D. Shi, Z. Budrikis, A. Stein, S. A. Morley, P. D. Olmsted, G. Burnell, and C. H. Marrows, Nat. Phys. **14**, 309 (2018).
[12] M. Saccone, A. Scholl, S. Velten, S. Dhuey, K. Hofhuis, C. Wuth, Y.-L. Huang, Z. Chen, R. V. Chopdekar, and A. Farhan, Phys. Rev. B **99**, 224403 (2019).
[13] M. Saccone, K. Hofhuis, D. Bracher, A. Kleibert, S. van Dijken, and A. Farhan, Nanoscale **12**, 189 (2020).
[14] Y.-L. Wang, Z.-L. Xiao, A. Snezhko, J. Xu, L. E. Ocola, R. Divan, J. E. Pearson, G. W. Crabtree, and W.-K. Kwok, Science **352**, 962 (2016).
[15] J. C. Gartside, D. M. Arroo, D. M. Burn, V. L. Bemmer, A. Moskalenko, L. F. Cohen, and W. R. Branford, Nat. Nanotechnol. **13**, 53 (2018).
[16] S. Gliga, A. Kákay, R. Hertel, and O. G. Heinonen, Phys. Rev. Lett. **110**, 117205 (2013).
[17] E. Östman, H. Stopfel, I.-A. Chioar, U. B. Arnalds, A. Stein, V. Kapaklis, and B. Hjörvarsson, Nat. Phys. **14**, 375 (2018).
[18] Y. Perrin, B. Canals, and N. Rougemaille, Phys. Rev. B **99**, 224434 (2019).
[19] V. Schánilec, B. Canals, V. Uhlíř, L. Flajšman, J. Sadílek, T. Šikola, and N. Rougemaille, Phys. Rev. Lett. **125**, 057203 (2020).
[20] G. H. Wannier, Phys. Rev. **79**, 357 (1950).
[21] R. L. Dally, Y. Zhao, Z. Xu, R. Chisnell, M. B. Stone, J. W. Lynn, L. Balents, and S. D. Wilson, Nat. Commun. **9**, 2188 (2018).
[22] P. Khuntia, M. Velazquez, Q. Barthélemy, F. Bert, E. Kermarrec, A. Legros, B. Bernu, L. Messio, A. Zorko, and P. Mendels, Nat. Phys. **16**, 469 (2020).
[23] S. Zhang, J. Li, I. Gilbert, J. Bartell, M. J. Erickson, Y. Pan, P. E. Lammert, C. Nisoli, K. K. Kohli, R. Misra, V. H. Crespi, N. Samarth, C. Leighton, and P. Schiffer, Phys. Rev. Lett. **109**, 087201 (2012).
[24] I. A. Chioar, N. Rougemaille, A. Grimm, O. Fruchart, E. Wagner, M. Hehn, D. Lacour, F. Montaigne, and B. Canals, Phys. Rev. B **90**, 064411 (2014).
[25] Y. Han, Y. Shokef, A. M. Alsayed, P. Yunker, T. C. Lubensky, and A. G. Yodh, Nature (London) **456**, 898 (2008).
[26] See Supplemental Material at http://link.aps.org/supplemental/10.1103/PhysRevLett.125.267203 for movie S1: XMCD image sequence of sample with a height offset $h = 280$ nm and lattice parameter $b = 475$ nm, recorded at 270 K and movie S2: XMCD image sequence of sample

with a height offset $h = 280$ nm and lattice parameter $b = 525$ nm, recorded at 250 K.

[27] U. B Arnalds, J. Chico, H. Stopfel, V. Kapaklis, O. Bärenbold, M. A. Verschuuren, U. Wolff, V. Neu, A. Bergman, and B. Hjörvarsson, New J. Phys. **18**, 023008 (2016).

[28] A. Vansteenkiste, AIP Adv. **4**, 107133 (2014).

[29] A. Doran, M. Church, T. Miller, G. Morrison, A. T. Young, and A. Scholl, J. Electron Spectrosc. Relat. Phenom. **185**, 340 (2012).

[30] J. Stöhr, Y. Wu, B. D. Hermsmeier, M. G. Samant, G. R. Harp, S. Koranda, D. Dunham, and B. P. Tonner, Science **259**, 658 (1993).

[31] A. Farhan, P. M. Derlet, A. Kleibert, A. Balan, R. V. Chopdekar, M. Wyss, J. Perron, A. Scholl, F. Nolting, and L. J. Heyderman, Phys. Rev. Lett. **111**, 057204 (2013).

[32] A. Farhan, C. F. Petersen, S. Dhuey, L. Anghinolfi, Q.-H. Qin, M. Saccone, S. Velten, C. Wuth, S. Gliga, P. Mellado, M. J. Alava, A. Scholl, and S. van Dijken, Nat. Commun. **8**, 995 (2017).

[33] D. Louis, D. Lacour, M. Hehn, V. Lomakin, T. Hauet, and F. Montaigne, Nat. Mater. **17**, 1076 (2018).

[34] Y. Qi, T. Brintlinger, and J. Cumings, Phys. Rev. B **77**, 094418 (2008).

[35] N. Rougemaille, F. Montaigne, B. Canals, A. Duluard, D. Lacour, M. Hehn, R. Belkhou, O. Fruchart, S. El Moussaoui, A. Bendounan, and F. Maccherozzi, Phys. Rev. Lett. **106**, 057209 (2011).

[36] A. Farhan, P. M. Derlet, L. Anghinolfi, A. Kleibert, and L. J. Heyderman, Phys. Rev. B **96**, 064409 (2017).

[37] P. E. Lammert, X. Ke, J. Li, C. Nisoli, D. M. Garand, V. H. Crespi, and P. Schiffer, Nat. Phys. **6**, 786 (2010).

[38] A. Farhan, A. Kleibert, P. M. Derlet, L. Anghinolfi, A. Balan, R. V. Chopdekar, M. Wyss, S. Gliga, F. Nolting, and L. J. Heyderman, Phys. Rev. B **89**, 214405 (2014).

[39] K. Motoya and K. Hioki, J. Phys. Soc. Jpn. **72**, 930 (2003).

[40] R. Witte, A. Sarkar, R. Kruk, B. Eggert, R. A. Brand, H. Wende, and H. Hahn, Phys. Rev. Mater. **3**, 034406 (2019).